



The effects of the microstructural characteristics of Fe–0.33C–1.2Mn–xNb–xMo steels on hydrogen embrittlement fracture

Mitsuhiro Okayasu · Ryo Arai · Takehide Senuma

Received: 11 May 2021 / Accepted: 11 August 2021 / Published online: 6 September 2021
© The Author(s), under exclusive licence to Springer Nature B.V. 2021

Abstract The hydrogen embrittlement (HE) characteristics of Fe–0.33C–1.2Mn–xNb–xMo steels were investigated experimentally using various samples with differing microstructural characteristics. HE in steels was affected by hydrogen trapping sites: ϵ -carbide-based, Nb-based, and Mo-based precipitates, which were effective at enhancing HE resistance. In contrast, the prior austenite (γ) grain boundary within steel could act as hydrogen trapping sites and accelerate HE. In addition, hydrogen trapping occurred around the crack, leading to an acceleration of crack growth rate. There are various trapping sites in the steels with negative and positive effects on HE. The extent of the HE was clarified via tensile strength and resistance of delayed failure. Furthermore, the HE characteristics were analyzed using the samples with different quantity of hydrogen charged with two different methods. Based upon the above work, high HE resistance of the steel was proposed as Fe–0.33C–1.2Mn–0.05Nb–0.5Mo steels after a bake-hardening process at 170 °C for 20 min.

Keywords Steel · Hydrogen embrittlement · Trapping site · Niobium carbide · Molybdenum carbide

1 Introduction

It is thought that one-third of all structural and component failure are caused by environmental effects, e.g., corrosion (Woodtli and Kieselbach 2000). Corrosion is a significant issue for the development of structures and components that are highly reliable for long periods. One related issue is affected by hydrogen: storage tank failure driven by the compressed hydrogen gas that it contained. This failure is attributed to rapid growth of large fatigue cracks and is induced by material embrittlement driven by hydrogen. It is well known that hydrogen is the lightest element and easily penetrates into metallic materials. This causes mechanical property deterioration and brittle fracture (West and Louthan 1979). To understand the phenomenon of hydrogen embrittlement (HE) in engineering materials, many researchers have examined the HE characteristics of steel materials. A search of the Scopus database indicated that more than 6400 academic papers were retrieved using a search for “hydrogen”, “embrittlement”, and “steel”. To solve this issue, hydrogen trapping sites can be created to prevent HE. Fe–C–Ti alloys have low HE resistance because they contain trapped hydrogen (Depover et al. 2015). There are several hydrogen trapping sites, including carbide base precipitates, dislocations, and phase boundaries (Choo and Lee 1982a; Chen et al. 2020). The activation energies for evolution of trapped hydrogen were determined experimentally from peak

M. Okayasu (✉) · R. Arai · T. Senuma
Graduate School of Natural Science and Technology,
Okayama University, 3-1-1 Tsushimanaka, Kita-ku,
Okayama 700-8530, Japan
e-mail: mitsuhiro.okayasu@utoronto.ca

temperatures measured at various heating rates. They were found to be 17.2 kJ mol^{-1} , 26.8 kJ mol^{-1} , and 35.2 kJ mol^{-1} at grain boundaries, dislocations, and supersaturated vacancies, respectively (Choo and Lee 1982b).

The resistance of delayed fracture of martensitic bolt steels were investigated by Yamasaki and Takahashi (Yamasaki and Takahashi 1997), where to determine the hydrogen amount for delayed failure, the relationship between critical content for delayed fracture (H_c) and environmentally penetrated content (H_E) in diffusible hydrogen was examined. The critical value (H_c) and the environmental value (H_E) were determined by accelerated delayed fracture tests under constant applied load.

Some precipitates can improve HE in steel. Fe_3C precipitates in quenched, tempered, high-strength steel can reduce HE due to their hydrogen trapping sites (Okayasu et al. 2020). Zhu et al. have reported improved HE associated with the trapping capacity of ε -carbide, as revealed using a three-dimensional atomic probe (Zhu et al. 2015). Furthermore, the effects of the hydrogen trapping abilities of Cr_{23}C_6 precipitates on the mechanical properties of cast Fe–C–Cr materials were investigated. It was found that the presence of carbides decreases HE susceptibility (Depover and Verbeken 2016). Ultra-high-strength (1700 MPa) steel suffers from HE in atmospheric corrosion environments, as hydrogen traps in this steel enhance hydrogen absorption (Li et al. 2010). Moreover, the resistance of this high-strength, low-alloy steel to hydrogen-induced cracking (HIC) can be improved via Nb microalloying (0.055 wt%). Steel with a few nanometer-size NbC precipitates exhibits a higher HIC resistance than steel with larger (100–200 nm) precipitates (Shiqi et al. 2018).

In contrast, some precipitates can accelerate brittle failure, i.e., severe HE. Ultra-low-carbon steel with copper added has a high resistance to low susceptibility to HE. There is more space available for hydrogen in carbon steel when ε -copper particles are precipitated. The ε -copper precipitates that grow are better hydrogen trapping sites than the copper clusters. This contributes to suppression of strength reduction (Komazaki et al. 2002). A related study was further conducted which found that the grain and phase boundaries in iron and steel can be hydrogen trapping sites. The ferrite/pearlite and pearlite/pearlite interfaces in pure Fe–C alloys are effective trapping sites,

while the ferrite/cementite interfaces within the pearlite colonies have little effect on the hydrogen occlusivity (Chan and Charles 1986). Enos and Scully explained that the shear-cracking process in cold-drawn ultrafine pearlitic steel is assisted by trapped hydrogen due to reduction of the cohesive strength of the Fe/ Fe_3C interface (Enos and Scully 2002).

From the above information, it is clear that various hydrogen trapping sites can change the extent of HE. Some precipitates can improve HE. However, the reason for this is not clear. Moreover, there is no clear direct evidence that can be used to understand the HE mechanism. Thus, the aim of the present study is to examine experimentally the HE characteristics in high strength steels with various microstructural formations, e.g., precipitates, phases and internal strain.

2 Experimental procedures

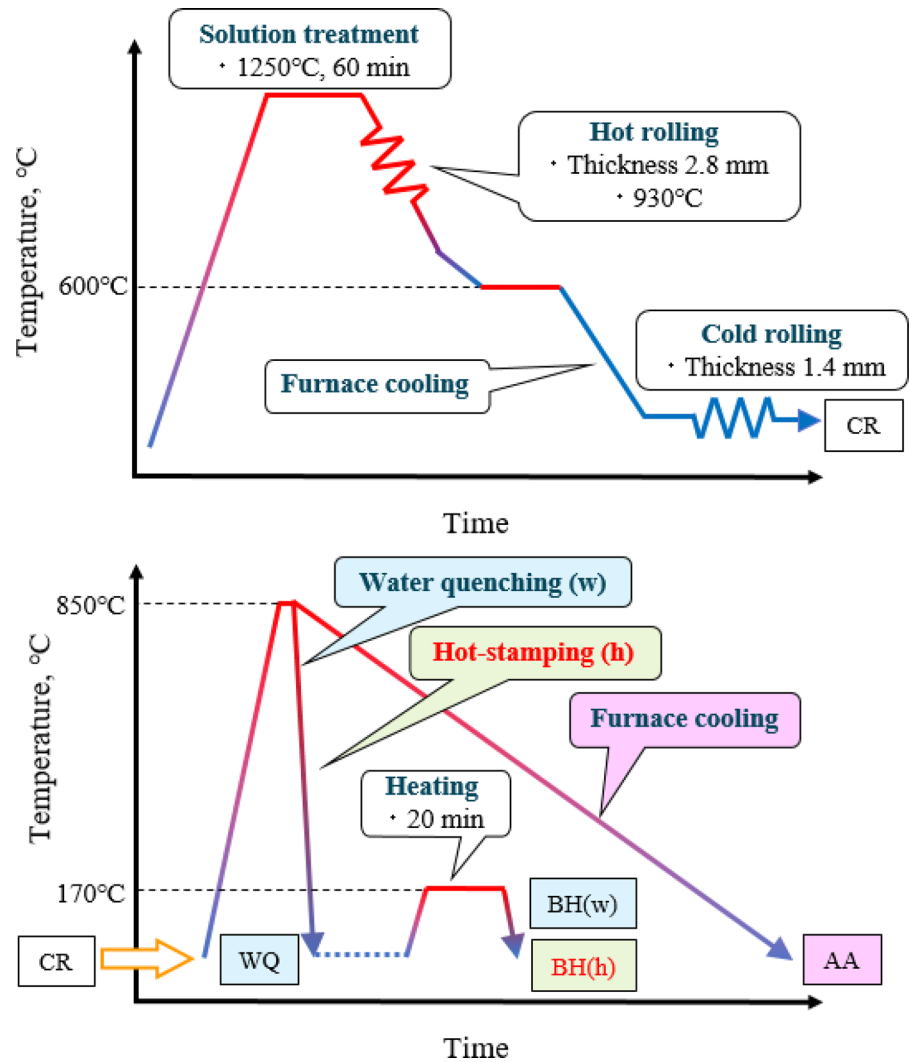
2.1 Materials and specimens

In this study, Fe–0.33C–1.2Mn–xNb–xMo (Fe–xNb–xMo) steels formed via cold rolling were used. Table 1 shows the chemical compositions of the steels. The concentrations of niobium (Nb) and molybdenum (Mo) varied between steels (Nb: 0% or 0.05 mass% and Mo: 0.15 mass%, 0.3 mass%, or 0.5 mass%). Figure 1 shows schematic illustrations of the sample preparation processes. The different processes were cold-rolling (CR), annealing (AA), quenching (WQ), and tempering (BH). The cold-rolling sample was manufactured with a thickness of 1.4 mm using a 2.8 mm hot-rolled sheet. AA was performed using a CR sample heated to 850 °C for 1 h before air cooling. The WQ process was performed in cold water after heating above the A_3 line (i.e., 800 °C) for 30 min, while the BH process was conducted by tempering at 170 °C for 20 min in an oil bath using two different samples: (i) water quenched [BH(w)] and (ii) hot stamped [BH(h)]. The hot-stamped samples were made by the hot pressed to make U-bent specimen. In the present study, the hot workpiece heated at 850 °C was rapidly cooled via die-clumping using a hydraulic mechanical servo press at a load of 60 tons, where the quenched/tempered dies made of commercial SKD11 tool steel were employed. Note that a glass coating processes were executed to each steel sample during heating so as to prevent decarburization.

Table 1 Chemical composition of the Fe-xNb-xMo steel (mass%)

	C	Mn	Si	Nb	Mo	P	S	Ti	Al	B	N
1	0.32	1.2	0.1	0	0	0.001	0.002	0.01	0.004	0.002	0.002
2	0.32	1.2	0.1	0.05	0	0.001	0.002	0.01	0.004	0.002	0.002
3	0.33	1.2	0.1	0	0.15	0.005	0.005	0.02	0.004	0.002	0.002
4	0.33	1.2	0.1	0	0.3	0.005	0.005	0.02	0.004	0.002	0.002
5	0.33	1.2	0.1	0	0.5	0.005	0.005	0.02	0.004	0.002	0.002
6	0.32	1.2	0.1	0.05	0.5	0.001	0.002	0.01	0.004	0.002	0.002

Fig. 1 Schematic illustration showing the sample preparation processes for the cold rolling (CR), water quenching (WQ), quenching and tempering [BH(w) and BH(h)], and annealing (AA)



2.2 Hydrogen charging

The HE characteristics of the steel samples were examined after hydrogen charging using two different methods: an ammonium thiocyanate (NH₄SCN) solution and an electric charging in 3 g L⁻¹

NH₄SCN + 3% NaCl at 10 A m⁻². The samples were ground with emery paper down to 800 grade and immersed at the room-temperature. Following hydrogen charging, the hydrogen content in the sample was measured by means of thermal desorption analysis using a gas chromatograph with a linear heating rate of

3.3 °C min⁻¹ to 400 °C. The sample gas was analyzed with a 5 min interval using argon as a carrier gas. In the present analysis, the hydrogen content detected around 100 °C is considered to be the diffusible hydrogen content (Okayasu and Yang 2019).

2.3 Mechanical testing

To understand the HE characteristics, the mechanical properties and resistance of delayed fracture were examined using the samples with hydrogen charged, where two different specimens were employed, e.g., dumbbell shaped specimen and U-bent specimen. Figure 2 shows the photographs of both test specimens. Tensile test specimens were frozen in liquid nitrogen to avoid hydrogen leakage from the test samples before the tensile testing. The tensile tests were performed using a screw-driven universal testing machine with a 50 kN capacity. The test specimens were loaded at 0.01 mm min⁻¹ and 1 mm min⁻¹ via

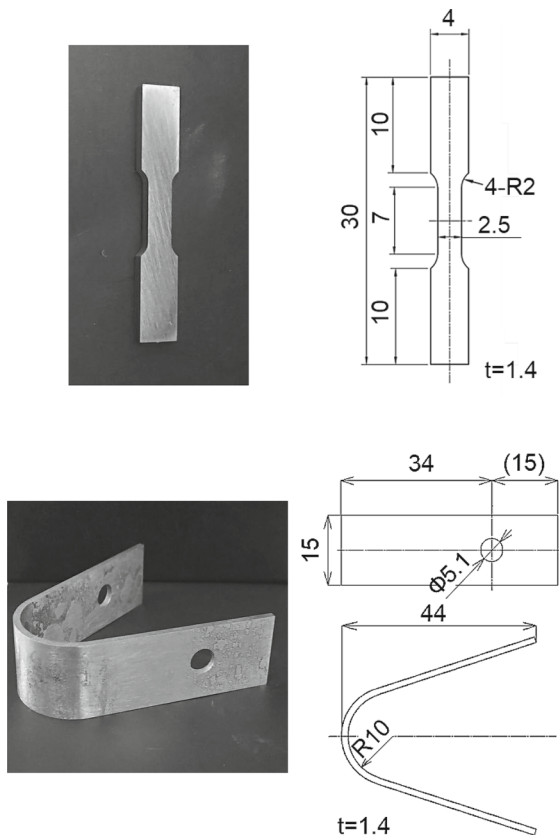


Fig. 2 Photographs and drawings of dumbbell shape and U-bent specimens for tensile and delayed fracture tests

Fig. 3 EBSD analyses of Fe-xNb-xMo steels showing the inverse pole figure and kernel average misorientation: AA, CR, WQ, and BH(w) samples

stroke control until the fracture point. The test specimens were designed to possess a rectangular dumbbell shape with dimensions of 30 mm × 4 mm × 1.4 mm. The resistance to delayed fracture was investigated using U-bent specimens under hydrogen charging. In this case, the delayed fracture tests were conducted under the two different methods: static loading of 1700 MPa and 1400 MPa in the NH₄SCN solution and the electric charging, respectively, where the U-bent specimen was tightly jointed using a bolt. The fracture resistance was evaluated on the basis of the time to final failure of the specimen. It should be pointed out that, in this case, the static loading values (1700 MPa and 1400 MPa) were selected, as the change of the fracture resistance was clearly obtained.

2.4 Microstructural analysis

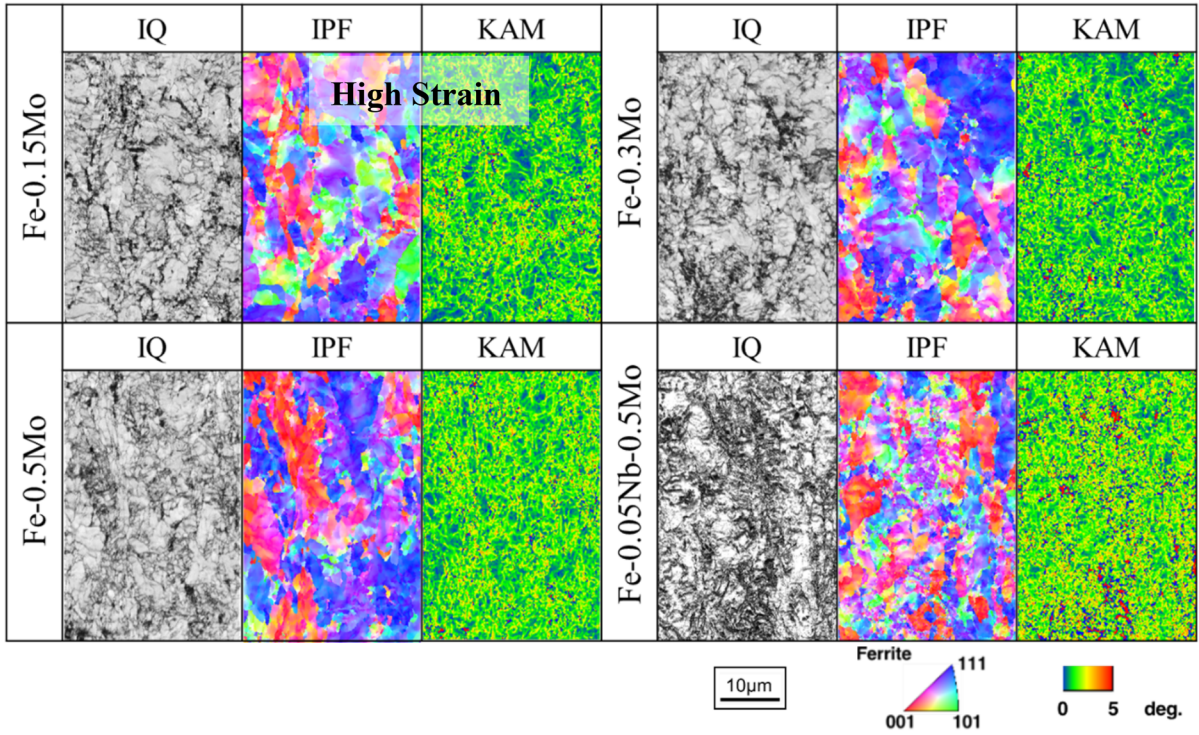
The microstructural characteristics of the steel samples were analyzed via electron backscatter diffraction (EBSD) analysis. EBSD analysis was conducted using a beam current 12 mA, an accelerating voltage 15 kV, and a step size 1 μm. The sample surfaces were polished mechanically to mirror status using a cloth with alumina particles. Furthermore, scanning transmission electron microscopy (STEM) and energy dispersive X-ray spectroscopy (EDS) analyses were performed to understand the precipitation characteristics of the steel in detail. For this, replica samples were prepared via mechanical thinning followed by electrolytic polishing with 10% perchloric acid and 90% ethanol.

3 Results

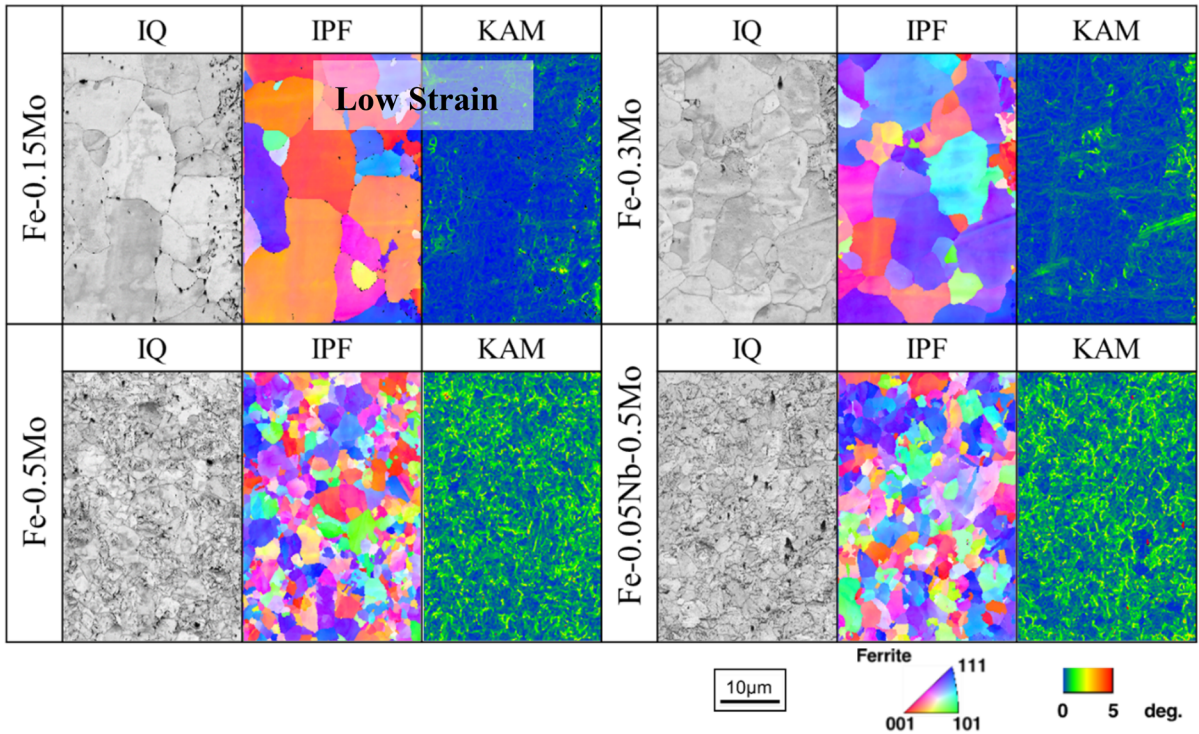
3.1 Mechanical properties

Figure 3 shows EBSD analysis results for Fe-xNb-xMo steels made using various processes with various Nb and Mo concentrations. The color levels of the pixels in the IPF maps vary according to the deviation from the measured crystal orientation. The KAM maps

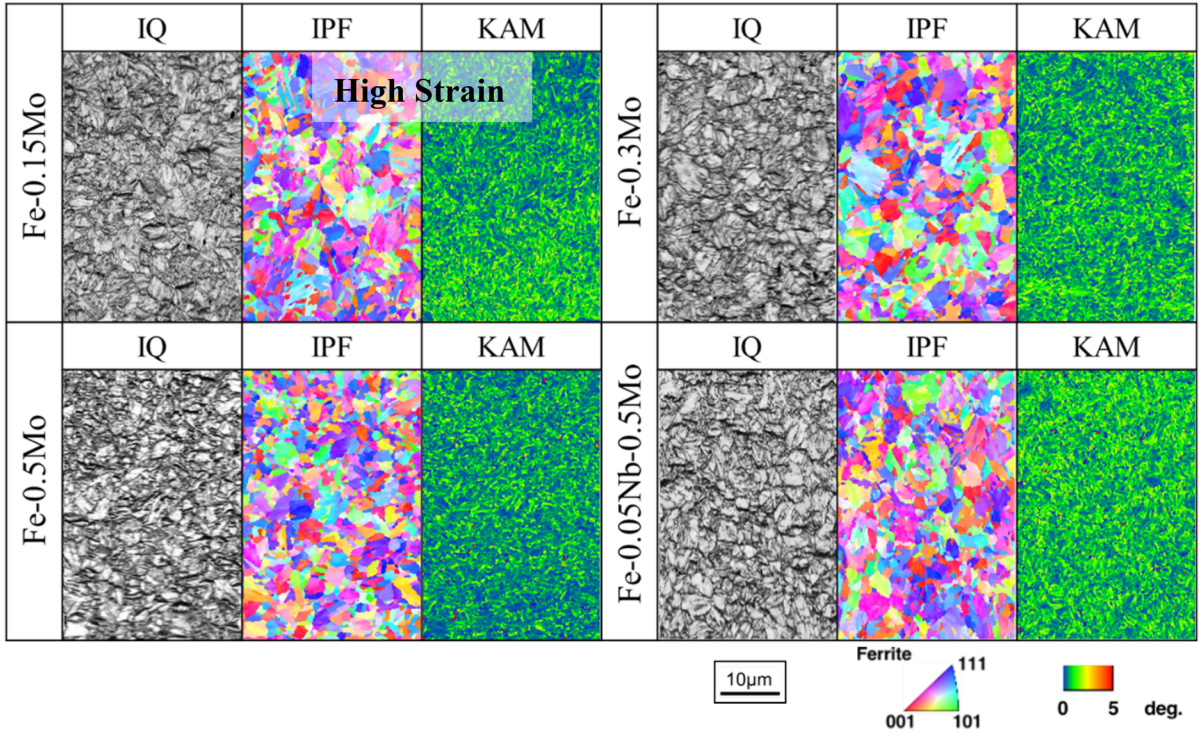
(a) CR



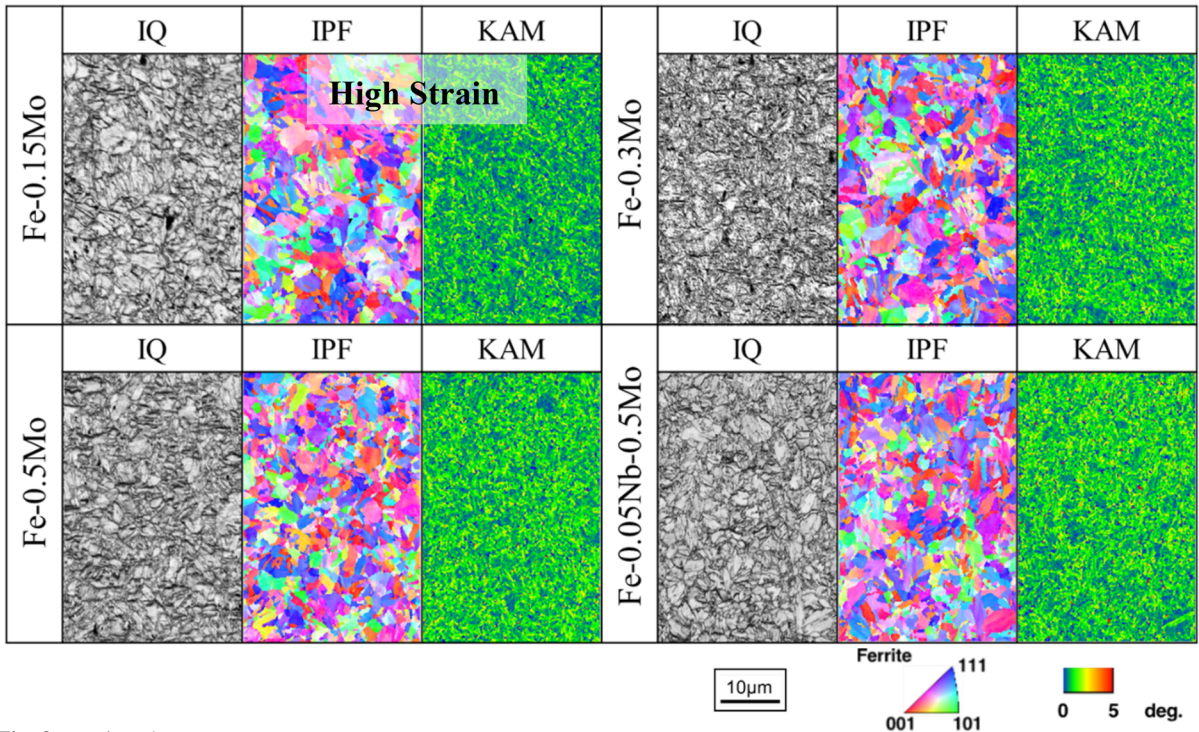
(b) AA



(c) WQ



(d) BH(w)



◀ Fig. 3 continued

indicate the mean misorientation angle of a given point against all of its neighbors, which is related to the extent of internal strain. The CR and AA samples are formed with ferrite (57%) and pearlite (43%) structures. Because of the cold-rolling process, the KAM levels are higher in the CR samples than in the AA samples. The grains appear strained in the former samples, as shown in the IPF maps. This results in higher hardness, i.e., work hardening. The low KAM level for AA is caused by the annealing process. The relatively high internal strains in the WQ and BH(w) samples occur because the martensite structure exhibits a high concentration of carbon solid solutions and severe ε -carbide precipitation. It is also clear that the grain sizes in the AA, WQ, and BH(w) samples decrease to almost same size as the amount of Nb and Mo increases. This leads to high mechanical strength (Okayasu et al. 2016), i.e., grain boundary strengthening. Because of the severe strain in the CR samples, grain-size differences are not noted. It should be pointed out that despite the BH process conducted, similar microstructural characteristics are seen in the WQ and BH(w).

3.2 Hydrogen embrittlement properties

Figure 4 shows the representative tensile stress versus tensile strain curves of CR, AA, WQ and BH(w) before and after their subjection to hydrogen charging for 48 h. From the S - S curves, different trends of the tensile properties were obtained. After yielding, the tensile stress decreases for CR, WQ and BH(w), while the tensile stress increases as work hardening for AA. Severe reduction of ductility was obvious for WQ and some BH(w) samples after the hydrogen charging although small reduction of the ductility is seen in the other samples. Figure 5 shows the tensile properties of the Fe- x Nb- x Mo steels before and after hydrogen charging obtained from their tensile stress vs. strain curves. Different samples exhibit different S - S curve trends: (i) the ultimate tensile strength (σ_{UTS}) increases slightly with the Mo content and (ii) higher σ_{UTS} values are observed for WQ and BH(w) overall, while CR and AA exhibit lower σ_{UTS} values. Upon hydrogen charging, HE appears to occur at a different level, which is related to their tensile properties. The fracture strain decreases for the CR, WQ, and BH(w) samples, but no clear change in the ε_f value is obvious for AA. In particular, a significant fracture

Fig. 4 Engineering tensile stress versus tensile strain for the Fe- x Nb- x Mo steels with and without hydrogen charging (AA, CR, WQ and BH)

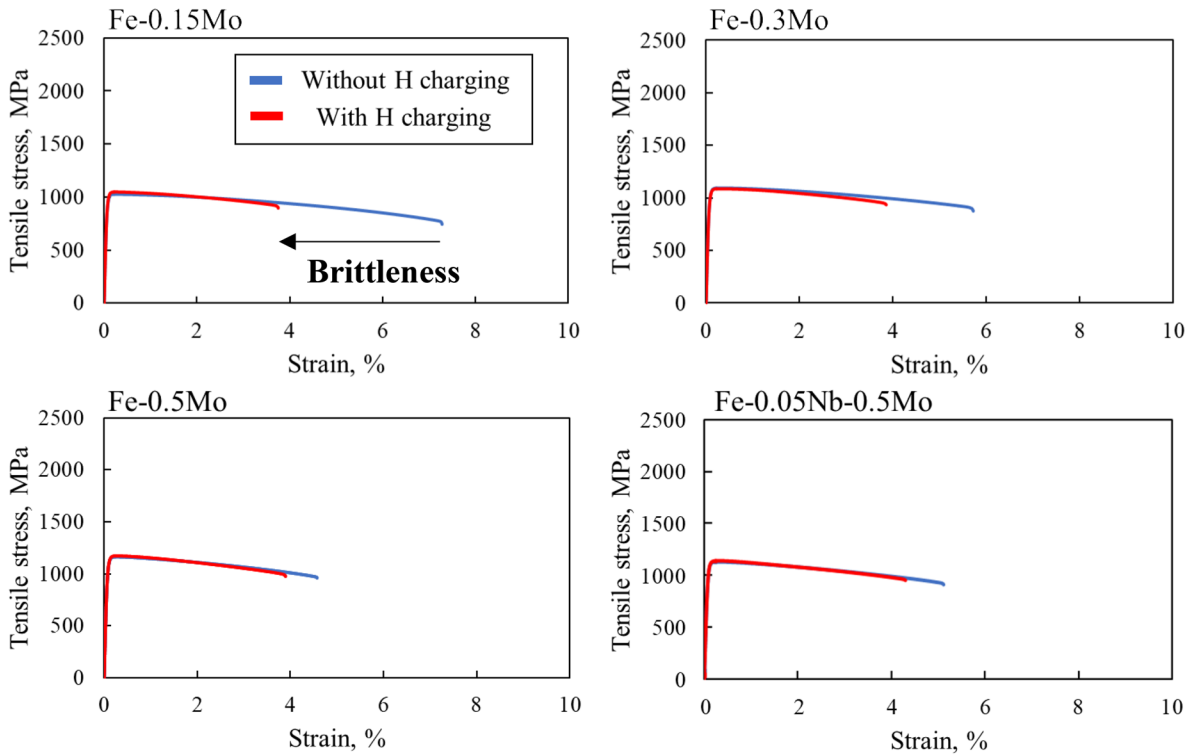
strain reduction occurs for WQ, where the fracture strain decreases due to failure in the elastic strain region. The strain reduction rate varies with the Mo content. HE improvements can be observed for BH(w), especially when the concentrations of additional chemical elements, e.g., BH(w)-0.5Mo and BH(w)-0.05Nb-0.5Mo, increase. Since WQ-Fe-0.05Nb-0.5Mo has a higher tensile strength than BH(w)-0.5Mo after hydrogen charging, higher HE resistance is observed using the Fe-Nb-Mo alloy.

It is also clarified from Fig. 5d that the high resistance of HE is obtained for BH(w)-0.05Nb-0.5Mo under the tensile loading at 0.01 mm min^{-1} , while the low resistance of HE for the other samples, loaded at 0.01 mm min^{-1} . The significant reduction of HE in the tensile properties at 0.01 mm min^{-1} is affected by a large amount of hydrogen penetrated to PAG (Okayasu and Motojima 2020). Because of no clear effect of HE for the BH(w)-0.05Nb-0.5Mo sample, other factors, such as creation of trapping sites and increment of interfacial strength of PAG, may have affected. It is considered from the above results that HE can be controlled by via addition of chemical elements (especially Nb and Mo) and heating processing.

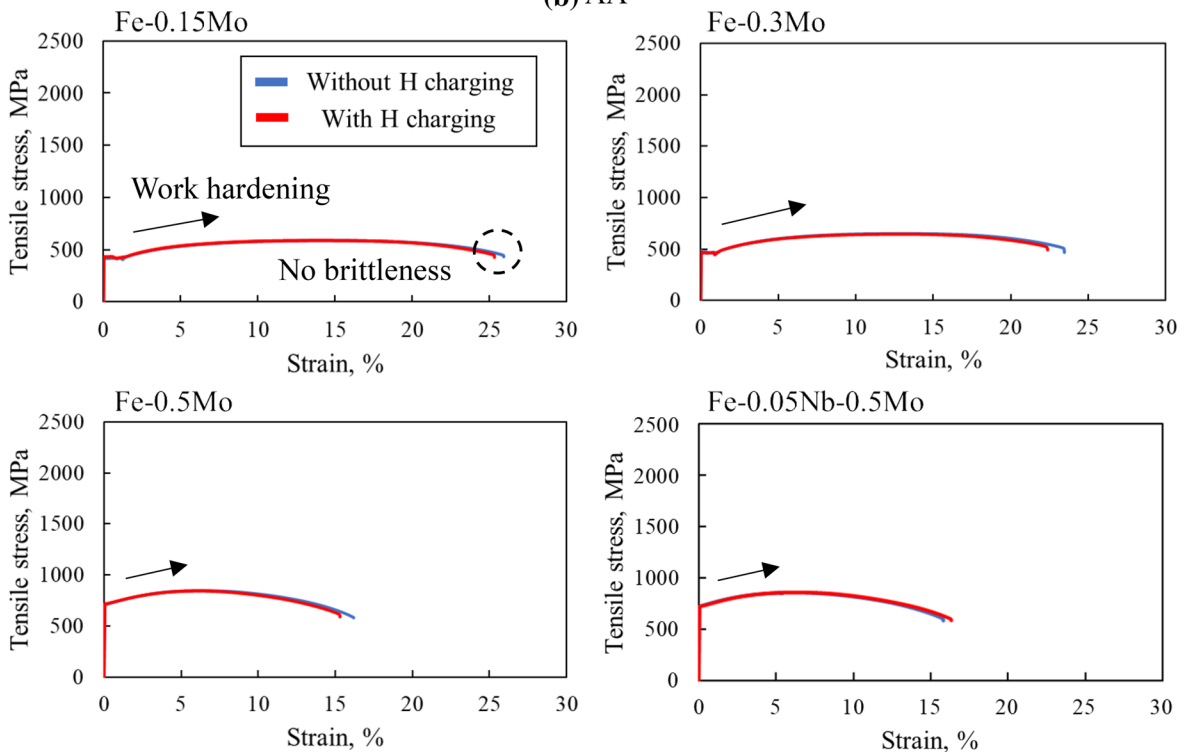
The extent of HE is sometimes attributed to various microstructural characteristics, i.e., differing trapping sites. The hydrogen traps in CR samples are associated with high-strain regions or high dislocation densities arising from the severe plastic deformation during the CR process, while WQ traps are found at the prior austenite (γ) grain (PAG) boundaries (Okayasu and Motojima 2020) besides dislocations. Since the BH process is performed using the WQ sample, HE improvements may be caused by hydrogen trapping site creation during thermal annealing at $170 \text{ }^\circ\text{C}$ for 20 min.

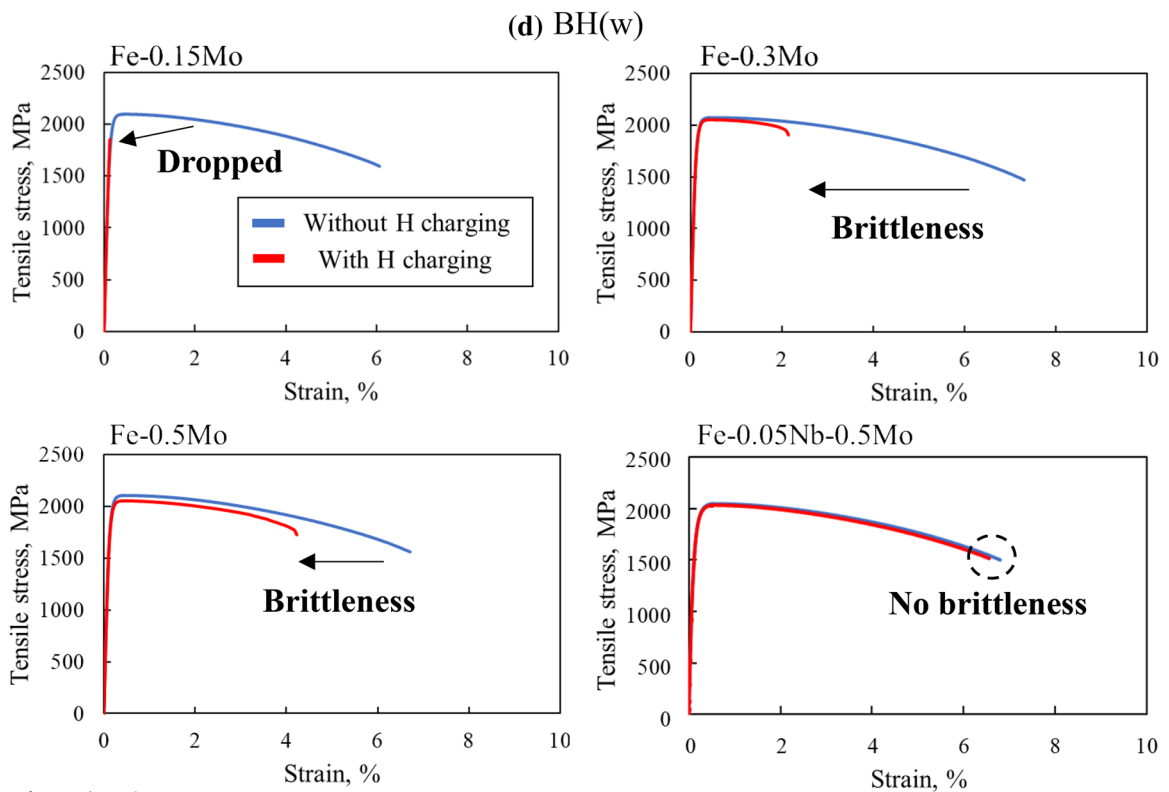
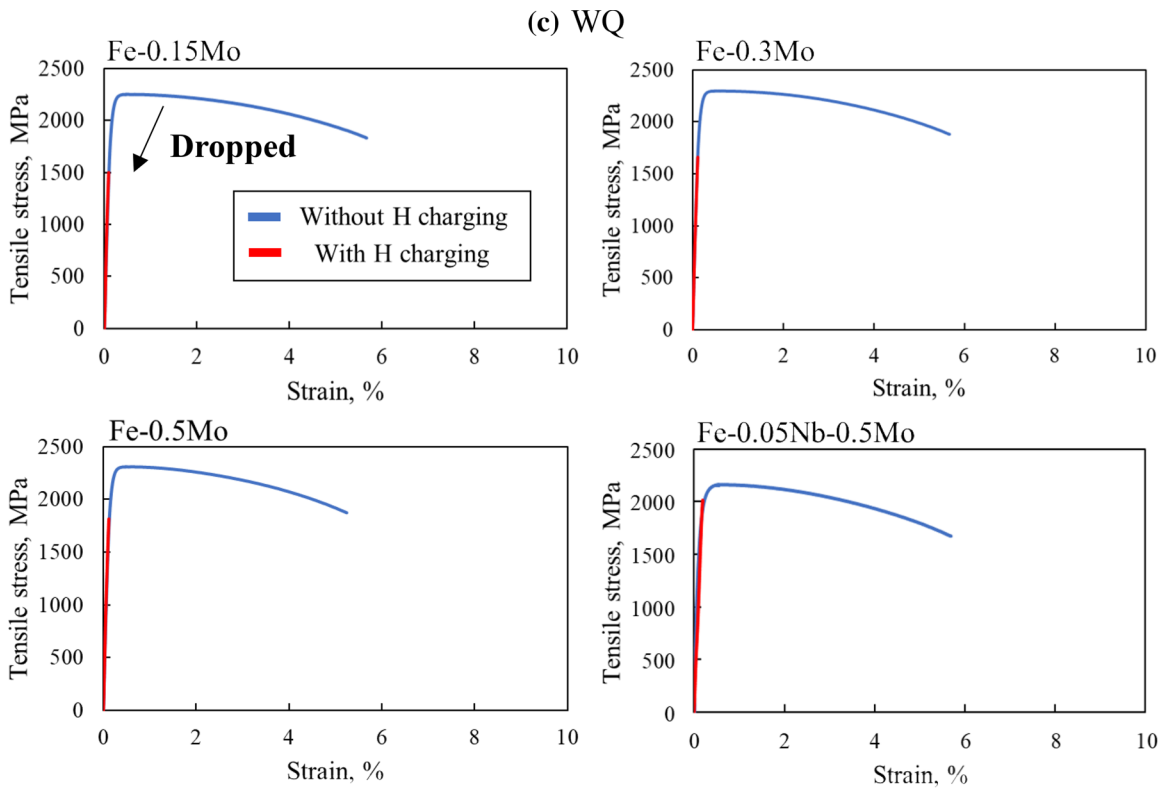
Figure 6a shows the results of the delayed fracture test for the BH(h) samples in NH_4SCN solution. It is seen that high fracture resistance is obtained for BH(h)-0.05Nb-0.5Mo, which is similar to the results of its tensile test. Note that some BH(h)-0.05Nb-0.5Mo specimens did not fracture even if the loading

(a) CR



(b) AA





◀ Fig. 4 continued

Fig. 5 Ultimate tensile strength (σ_{UTS}) and fracture strain (ϵ_f) results for Fe–xNb–xMo steels [AA, CR, WQ, and BH(w)] with and without hydrogen charging

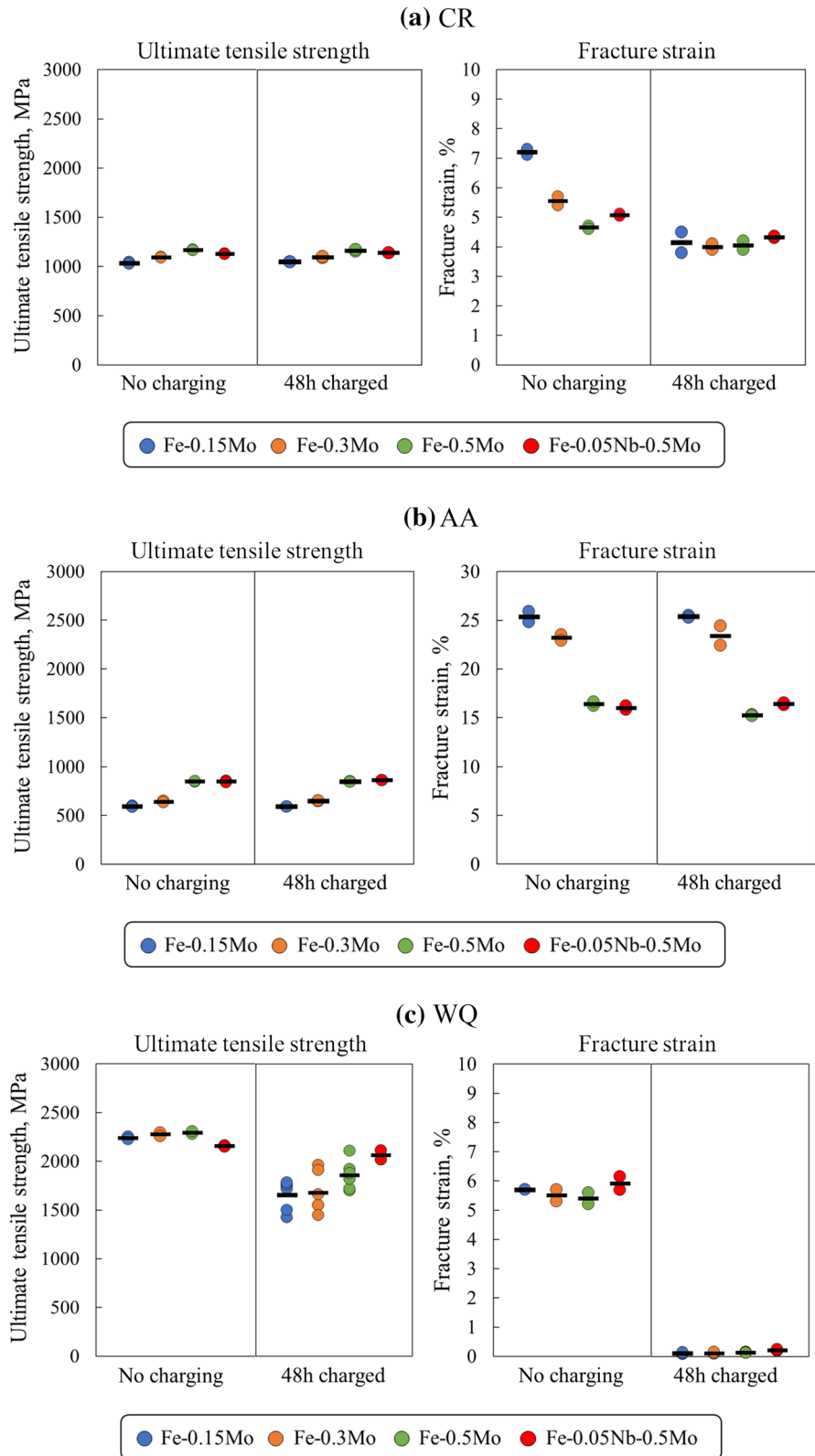
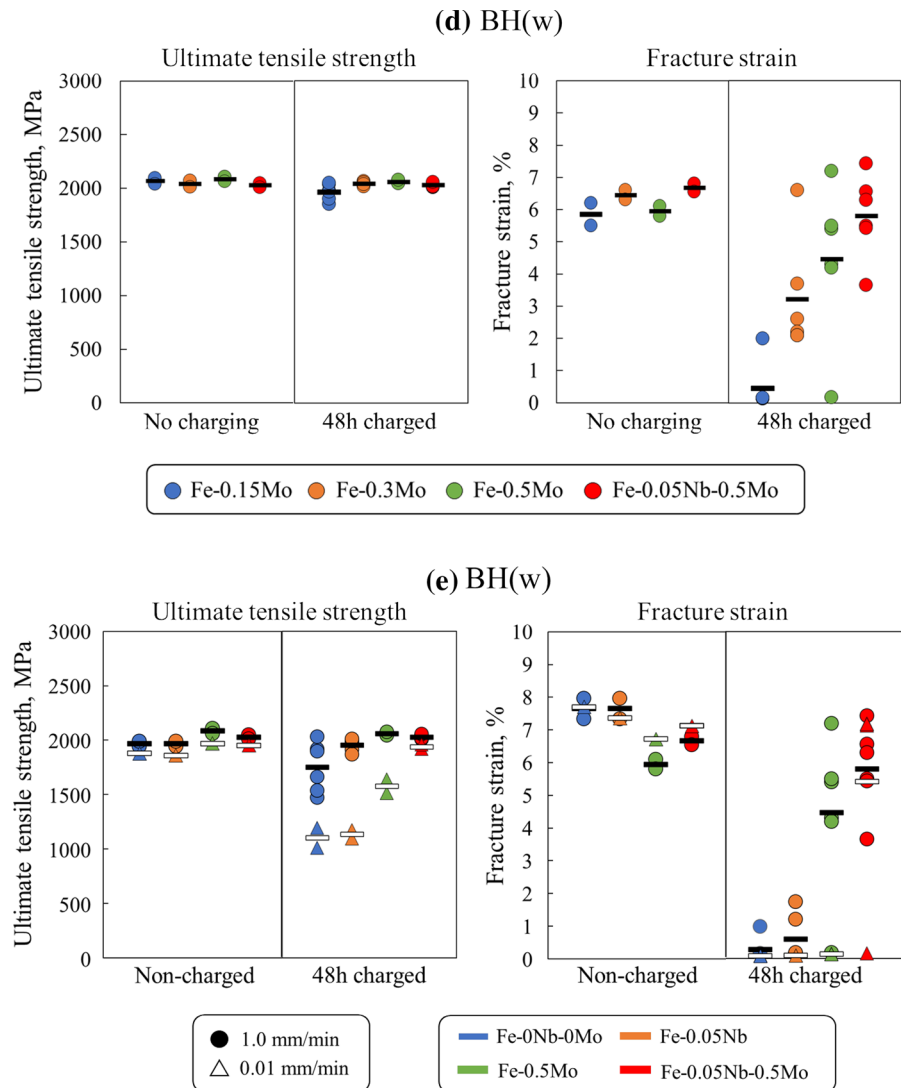


Fig. 5 continued



for more than 168 h. On the other hand, the low fracture resistance is detected for BH(h)-0Nb-0Mo alloys, while slight improvement of delayed fracture is seen for BH(h)-0.05Nb. The relatively high resistance of delayed fracture is obtained for BH(h)-0.5Mo. Such change of the fracture resistance would be affected by the different trap site of the BH(h) samples.

Figure 6b shows the results of resistance of delayed fracture for the BH(h) samples under the electric hydrogen charging. Dissimilar to the result of Fig. 6a, all samples were fractured in the early loading stage of around 20 h, including the BH(h)-0.05Nb-0.5Mo sample. The reason for this is not clear at the moment, but this could be attributed to the large amount of

hydrogen penetrated to the samples. Namely, the similar resistance of delayed fracture is caused by the similar hydrogen trapping in the PAG boundaries for all samples due to electric hydrogen charging.

Figure 6c displays the failure characteristics of the U-bent specimen under delayed fracture test for the BH(h) samples in NH_4SCN solution. As seen, the crack growth can be observed, in which the rapid crack growth occurs to final failure immediately after the crack generation. This crack growth rate can be much higher than that under the creep crack growth rate. In the previous work by Tabuchi et al. (1991), they have examined the creep crack growth in the Cr-Mo-V steel at high temperature, where the creep crack

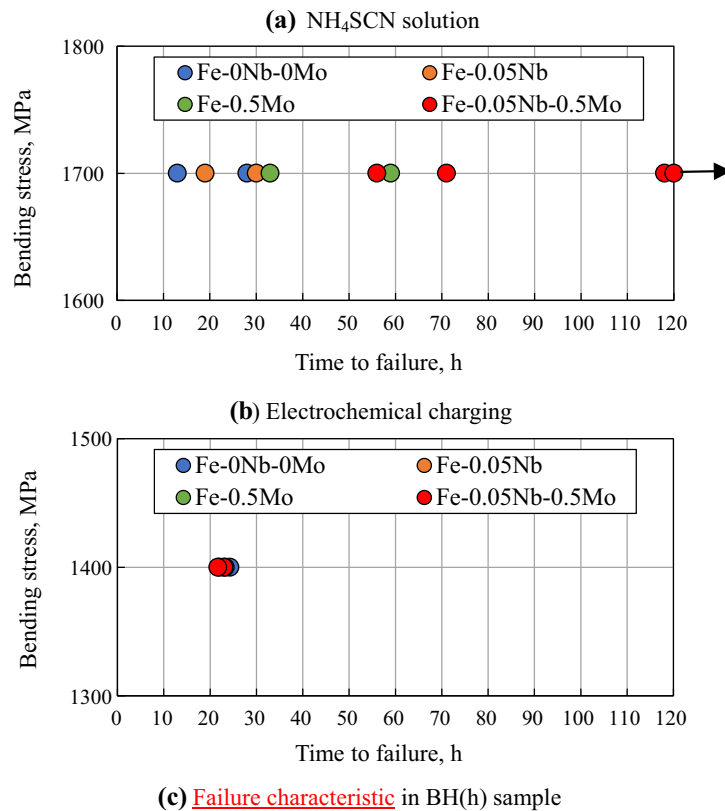


Fig. 6 **a** and **b** The relationship between the applied static stress and time to failure for BH(h) samples: **a** NH₄SCN solution and **b** electrochemical charging. **c** photographs of BH(h) specimens showing failure characteristics in NH₄SCN solution

growth in the tertiary creep stage is less than 1 mm h⁻¹.

4 Discussion

4.1 Failure analysis

Figure 7 shows SEM images of fracture surfaces of Fe-xNb-xMo steels prepared via the WQ and BH(w) processes after tensile testing. Examination of these fracture surfaces reveals various failure characteristics. It is clear from Fig. 7a that dimple- and slip-based ductile failures with severely necked samples are the dominant features in WQ and

BH(w) samples that have not been subjected to hydrogen charging. Such ductile fracture become brittle failure modes after hydrogen charging, which exhibits severe HE driven by intergranular cracking along the PAG boundary, as shown in Fig. 7b. This may be influenced by hydrogen trapping at PAG boundaries and/or hydrogen atoms from interstitial positions to neighboring atomic vacancies to prior austenitic boundaries due to dislocation movement. As shown in Fig. 7b, ductile failure is obvious in all BH(w) samples even after hydrogen charging. In particular, severe ductile necking failure is observed in the BH(w)-0.05Nb-0.5Mo samples. This is reflected in their HE improvements via the BH process and upon addition of alloying Nb and Mo.

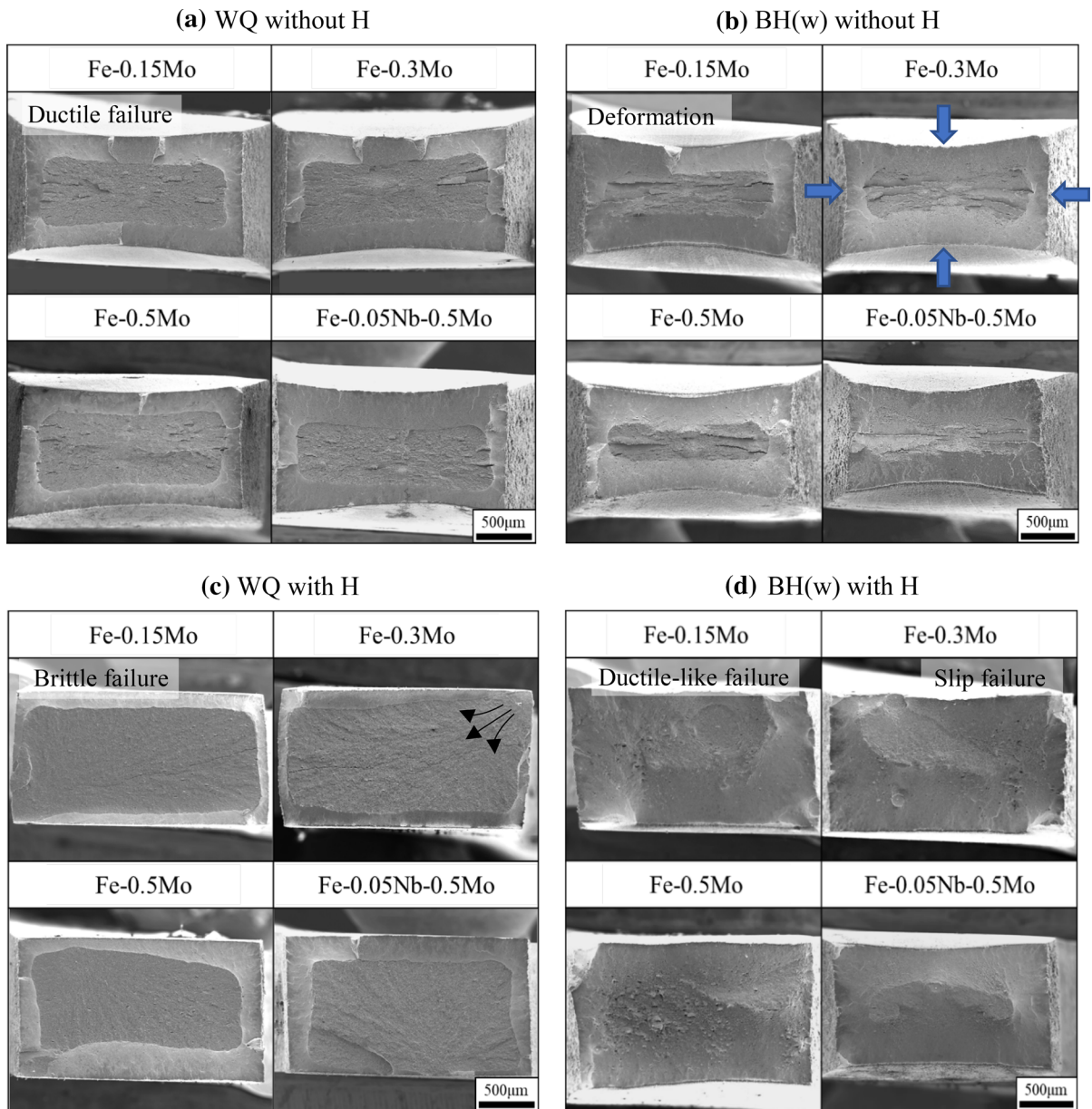


Fig. 7 SEM images of Fe- x Nb- x Mo steel fracture surfaces: WQ and BH(w) samples **a** without and **b** with hydrogen charging by NH_4SCN solution

Figure 8a, b displays variation in the cumulative hydrogen content with temperature and the variation of the amount of hydrogen released for representative CR, AA, WQ, and BH(w) samples (Fe-0.5Mo and Fe-0.05Nb-0.5Mo alloys) after 48 h of hydrogen charging using NH_4SCN solution. Extensive hydrogen is released upon heating to approximately 120 °C. This may be due to diffusible hydrogen. Interestingly,

diffusible hydrogen in the CR sample exhibits more than WQ although that for WQ is higher for the BH(w) and AA ones. It should be pointed out that severe HE occurred for WQ as described above although the lower amount of hydrogen is detected compared to that for CR. This result indicates different hydrogen trapping system in CR and WQ. In this case, the trapping sites in CR may have weak effects on HE,

while trapping sites at the PAG boundaries for WQ make stronger effects. It is also considered the different hydrogen trapping site in the AA and BH samples, due to their different microstructural characteristics: the trapping site could be the boundaries between cementite and ferrite for AA; while that is caused mainly by the precipitates for BH.

Figure 8c, d shows variation in the cumulative hydrogen content with temperature and the variation of the amount of hydrogen released for representative BH-Fe-xNb-xMo alloys after hydrogen charging by NH₄SCN solution and electric charging. Although the amount of hydrogen is scattered, a large amount of hydrogen is obtained for all samples after the electric charging, compared to that after NH₄SCN charging. It is considered from this result that the hydrogen charging at all trapping sites occur severely by the electric charging process, resulting in the high HE for all samples. Moreover, the temperature of extensive hydrogen released is different depending on the samples, e.g., 80–120 °C, e.g., Fig. 8d. This could be attributed to the different trapping sites.

4.2 Microstructural analysis

To explain the different severities of HE in the WQ and BH(w) samples, their microstructural characteristics were investigated in detail via STEM analysis. Figure 9a shows STEM images of the WQ-0.5Mo, BH(w)-0.5Mo, and BH(w)-0.05Nb-0.5Mo samples. Conventional lath martensite structures are observed for the three samples, while some precipitation particles are observed randomly in the martensite structures. These include ϵ -carbide-, Mo-, and Nb-based precipitates. The precipitate size and quantity in the BH(w)-0.5Mo sample are similar to those in the BH(w)-0.05Nb-0.5Mo sample, although weak precipitates are clearly visible in the WQ sample.

It is also clear from the STEM-EDX mapping in Fig. 9b that Ti-Mo-Nb-based precipitates are detected in the BH(w)-0.05Nb-0.5Mo samples. These precipitates could be related to (Ti, Nb)C and (Ti, Nb, Mo)C (Jang et al. 2013). The HE improvements noted in the BH(w) samples upon addition of Nb, Mo, and C indicate that ϵ -carbide and/or Nb- and Mo-based precipitates could act as hydrogen trapping sites and generate high HE resistance. Moreover, the reduction of internal strain after the BH(w) process may reduce the HE, as mentioned in Fig. 3. As in Fig. 8b, the

Fig. 8 Variation in the cumulative hydrogen content with temperature for **a** Fe-0.5Mo and **b** Fe-0.05Nb-0.5Mo steels [AA, CR, WQ, and BH(w)] after hydrogen charging with NH₄SCN solution; and BH(w)-Fe-xNb-xMo steels after hydrogen charging with **c** NH₄SCN solution and **d** electrochemical charging

quantity of hydrogen varies between samples. In this case, the maximum quantity of diffusivity hydrogen for the BH(w)-0.05Nb-0.5Mo samples is as low as approximately 0.01 ppm, which could be caused by the hydrogen trapping mainly in the precipitates mentioned above.

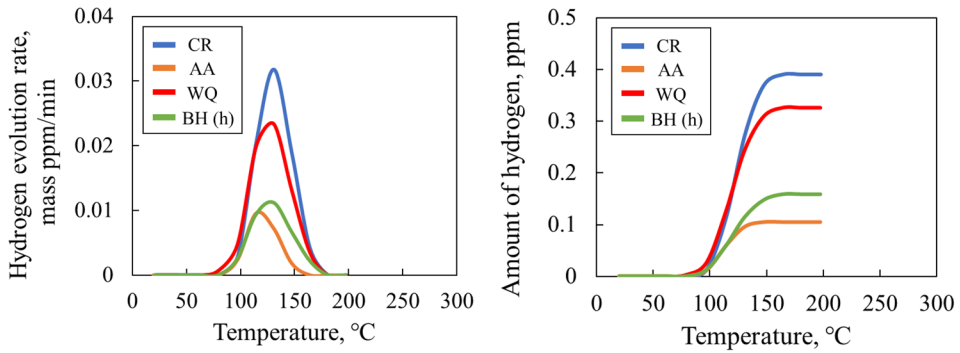
Based upon the material properties as mentioned above, the HE characteristics of the WQ and BH samples are understood using models. Figure 10 shows schematic diagrams of the HE models for the WQ-0Nb-0Mo and BH-0.05Nb-0.5Mo samples. Severe HE occurred in the WQ sample due to hydrogen trapping at the boundaries of the PAGs; moreover, a large amount of hydrogen migrated to around the crack makes increment of the HE. On the other hand, an improvement of HE was affected by the trapping sites of Nb-, Mo-based precipitates and ϵ -carbide. Furthermore, increasing the cohesive strength of the PAG boundaries may have also led to the high resistance of the delayed failure although there is no direct evidence.

5 Conclusions

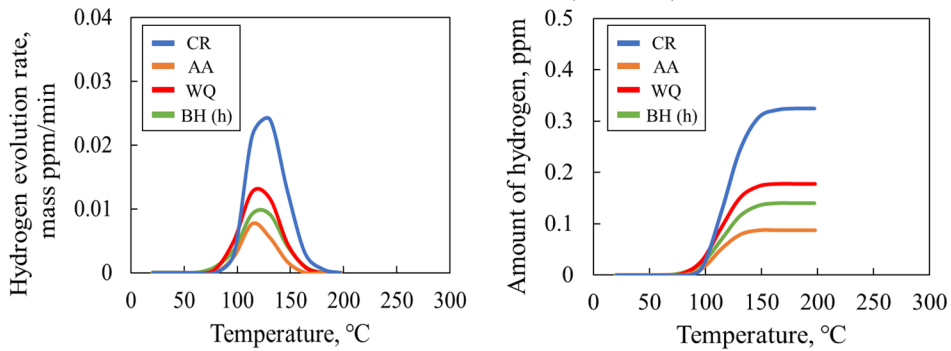
The effects of the microstructural characteristics of Fe-0.33C-1.2Mn-xNb-xMo steels on HE properties were examined using various samples with different microstructural characteristics, including different phase structures and precipitates. The results can be summarized as follows:

- (1) Nb and Mo could generate Nb- and Mo-based precipitates during the water quenching (WQ) and tempering processes (BH). In addition, ϵ -carbide precipitates were observed in the WQ and BH samples. These precipitates could be hydrogen trapping sites and reduced the severity of HE. The BH process improved HE, as both severe precipitation and internal strain were reduced. The improvement of HE was verified by the tensile test and delay fracture test.

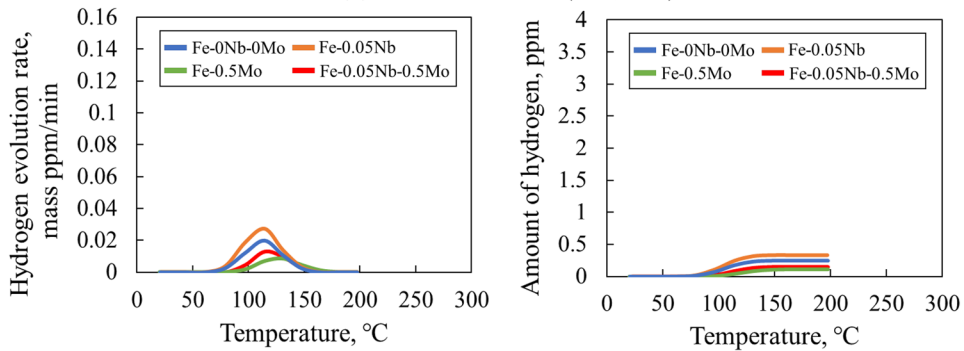
(a) Fe-0.5Mo (NH₄SCN)



(b) Fe-0.05Nb-0.5Mo (NH₄SCN)



(c) BH-Fe-xNb-xMo (NH₄SCN)



(d) BH-Fe-xNb-xMo (electrochemical charging)

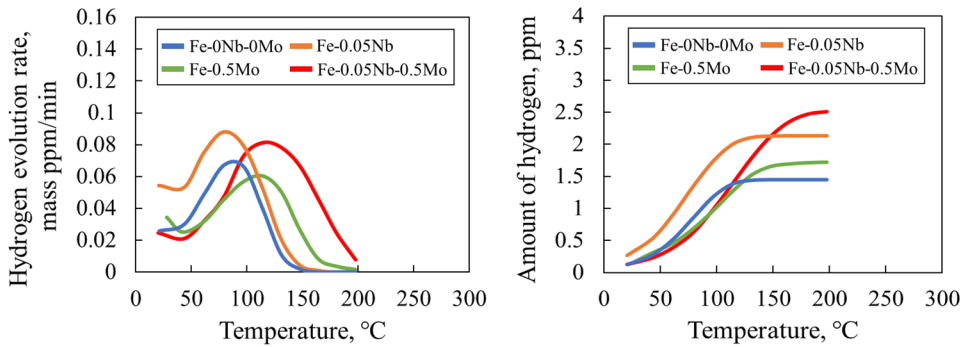
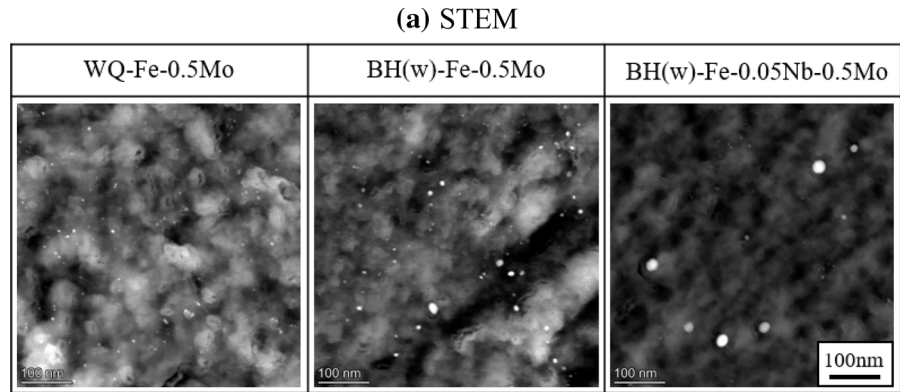
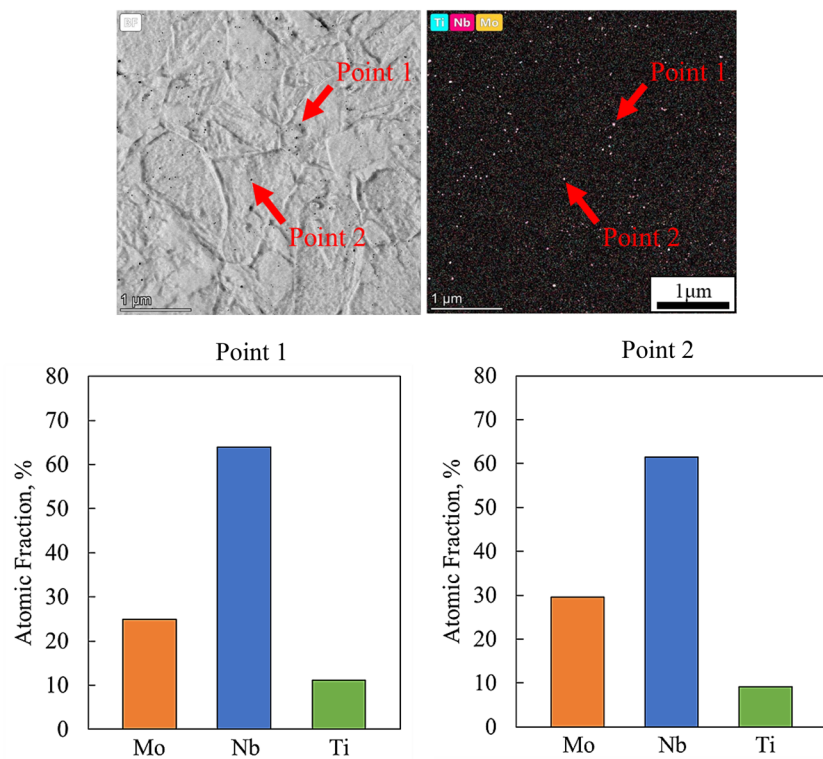


Fig. 9 **a** STEM images of the WQ-0.5Mo, BH(w)-0.5Mo, and BH(w)-0.05Nb-0.5Mo steels showing ϵ -carbide, Nb- and Mo-based precipitates. **b** STEM images and EDX maps of precipitates in BH(w)-0.05Nb-0.5Mo steel



(b) EDS (BH(w)-Fe-0.05Nb-0.5Mo)

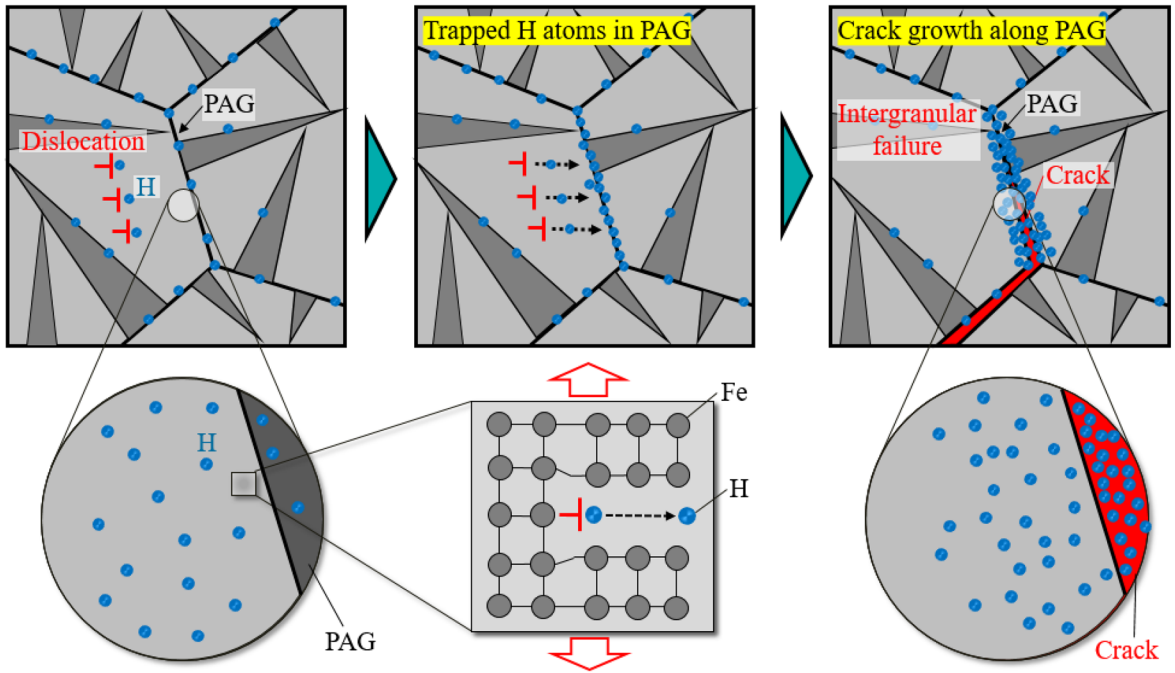


- (2) No clear HE was seen among AA samples, in which the hydrogen could be trapped between the cementite and ferrite phases. HE was also low among CR samples despite their high hydrogen contents. Hydrogen could be trapped at dislocations and internal lattice strain in CR samples, which makes weaker HE effects than the PAG boundaries in WQ.
- (3) The crack growth occurred rapidly to final failure immediately after the crack generation.

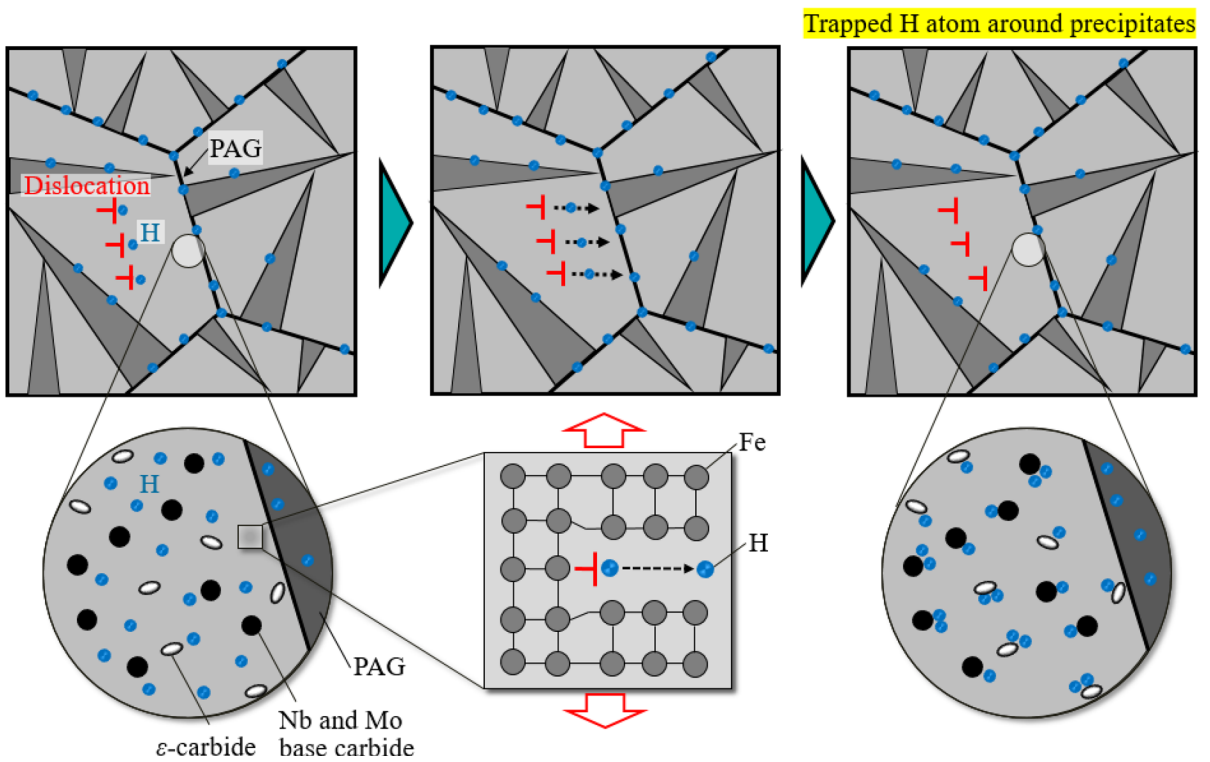
Such crack growth rate was much higher than the creep crack growth in the Cr-Mo-V steel at high temperature, less than 1 mm h^{-1} .

- (4) Hydrogen content in the BH-Fe-0.05Nb-0.5Mo alloys after the electric hydrogen charging in $3 \text{ g L}^{-1} \text{ NH}_4\text{SCN} + 3\% \text{ NaCl}$ at 10 A m^{-2} was more than 3 times higher than that charged by

(a) WQ-0Nb-0Mo sample



(b) BH-0.05Nb-0.5Mo samples



◀ **Fig. 10** HE models for the WQ-0Nb–0Mo and BH-0.05Nb–0.5Mo samples in consideration of the influences of precipitates and PAG as hydrogen trapping sites

NH₄SCN solution. The high hydrogen content made an acceleration of the delayed failure. Such severe HE was similarly observed for all sample after the electric charging.

Acknowledgements This research was carried out as a part of a project of the Commission Business Future Exploitation Research Program administered by the New Energy and Industrial Technology Development Organization (NEDO), Japan.

Declarations

Conflict of interest The authors declare no conflict of interest.

References

- Chan SLI, Charles JA (1986) Effect of carbon content on hydrogen occlusivity and embrittlement of ferrite-pearlite steels. *Mater Sci Technol* 2:956–962
- Chen Y-S, Lu H, Liang J, Rosenthal A, Liu H, Sneddon G, McCarroll I, Zhao Z, Li W, Guo A, Cairney JM (2020) Observation of hydrogen trapping at dislocations, grain boundaries, and precipitates. *Science* 367:171–175
- Choo WY, Lee JY (1982a) Hydrogen trapping phenomena in carbon steel. *J Mater Sci* 17:1930–1938
- Choo WY, Lee JY (1982b) Thermal analysis of trapped hydrogen in pure iron. *Metall Trans A* 13A:135–140
- Depover T, Verbeken K (2016) Hydrogen trapping and hydrogen induced mechanical degradation in lab cast Fe–C–Cr alloys. *Mater Sci Eng A* 669:134–149
- Depover T, Monbaliu O, Wallaert E, Verbeken K (2015) Effect of Ti, Mo and Cr based precipitates on the hydrogen trapping and embrittlement of Fe–C–XQ&T alloys. *J Hydrog Energy* 40:16977–16984
- Enos DG, Scully JR (2002) A critical-strain criterion for hydrogen embrittlement of cold-drawn, ultrafine pearlitic steel. *Metall Mater Trans A* 33A:1151–1166
- Jang JH, Heo Y-U, Lee C-H, Bhadeshia HKDH, Suh D-W (2013) Interphase precipitation in Ti–Nb and Ti–Nb–Mo bearing steel. *Mater Sci Technol* 29:309–313
- Komazaki S, Koyama A, Misawa T (2002) Effect of morphology of copper precipitation particles on hydrogen embrittlement behavior in Cu-added ultra low carbon steel. *Mater Trans* 43:2213–2218
- Li S, Akiyama E, Yuuji K, Tsuzaki K, Uno N, Zhang B (2010) Hydrogen embrittlement property of a 1700-MPa-class ultrahigh-strength tempered martensitic steel. *Sci Technol Adv Mater* 11:025005
- Okayasu M, Motojima J (2020) Microstructure-dependent hydrogen diffusion and trapping in high-tensile steel. *Mater Sci Eng A* 790:139418
- Okayasu M, Yang L (2019) Influence of microstructure on the mechanical properties and hydrogen embrittlement characteristics of 1,800 MPa grade hot-stamped 22MnB₅ steel. *J Mater Sci* 54:5061–5073
- Okayasu M, Wu S, Noda K, Lin D-Y, Yang S-M (2016) Mechanical properties of austenitic stainless steel with high niobium contents. *Mater Sci Technol* 32:1382–1394
- Okayasu M, Sato M, Ishida D, Senuma T (2020) The effect of precipitations (NbC and carbide) in Fe–C–Mn–xNb steels on hydrogen embrittlement characteristics. *Mater Sci Eng A* 791:139598
- Shiqi Z, Endian F, Jifang W, Jing L, Yunhua H, Xiaogang L (2018) Effect of Nb on the hydrogen-induced cracking of high-strength low-alloy steel. *Corros Sci* 139:83–96
- Tabuchi M, Kubo K, Yagi K (1991) Effect of specimen size on creep crack growth rate using ultra-large CT specimens for 1Cr–Mo–V steel. *Eng Fract Mech* 40:311–321
- West AJ, Louthan MR Jr (1979) Dislocation transport and hydrogen embrittlement. *Metall Trans A* 20:1675–1682
- Woodtli J, Kieselbach R (2000) Damage due to hydrogen embrittlement and stress corrosion cracking. *Eng Fail Anal* 7:427–450
- Yamasaki S, Takahashi T (1997) Evaluation method of delayed fracture property of high strength steels. *Tetsu-to-Hagane* 83:454–459
- Zhu X, Li W, Hsu TY, Zhou S, Wang L, Jin X (2015) Improved resistance to hydrogen embrittlement in a high-strength steel by quenching–partitioning–tempering treatment. *Scr Mater* 97:21–24

Publisher's Note Springer Nature remains neutral with regard to jurisdictional claims in published maps and institutional affiliations.